ChemSusChem

Research Article
doi.org/10.1002/cssc.202301866

Chemistry Europe
European Chemical Societies Publishing

www.chemsuschem.org

Understanding the Solid-Electrolyte-Interface (SEI) Formation in Glyme Electrolyte Using Time-Of-Flight Secondary Ion Mass Spectrometry (ToF-SIMS)

Chinmayee Padwal,[a, b] Hong Duc Pham,*[c] Linh Thi My Hoang,[a] Sagadevan Mundree,[d] Ashok Kumar Nanjundan,[e] Syam G. Krishnan,[f] and Deepak Dubal*[a, b]

Lithium-ion batteries are commonly used for energy storage due to their long lifespan and high energy density, but the use of unsafe electrolytes poses significant health and safety concerns. An alternative source is necessary to maintain electrochemical efficacy. This research demonstrates new safe glyme-based electrolytes for silica/carbon (SiO_x/C) nanocomposite derived from Australian rice husk (RH). The quality of SiO_x/C was preserved by using deep eutectic solvent-based pre-treatment and single-step carbonization, which was confirmed through the X-ray analysis of the crystalline phase of silica. The electrochemical assessment of SiO_x/C anode using various glyme-based electrolytes for LIBs was carried out. Among them, the resultant half cells based on diglyme electrolyte is superior to others with the first discharge capacity at 1274 mAh/g and a reversible discharge capacity of 759.7 mAh/g. Ex-situ SEM and Time-of-Flight Secondary Ion Mass Spectrometry (ToF- SIMS) analysis of the electrode indicated that diglyme not only improves the capacity but also sustains the electrode architecture for longer cycle life with more LiF-based components and also showed the absence of HF components. Importantly, the addition of fluoroethylene carbonate (FEC) additive enhanced the cycling stability. These results provide a new perspective on developing advanced SiOx/C anode using glyme electrolytes for Li-ion batteries.

1. Introduction

As the demand for energy storage devices continues to rise, lithium-ion batteries (LIBs) have emerged as a promising solution due to their high energy density and long cycle life. In terms of electrochemical performance in LIBs technology, the role of anodic materials is significant. Apart from conventional graphite-based anode materials, silicon in recent years has been intensively employed since its high theoretical capacity (~4000 mAh/g).[1,2] Nevertheless, their practical applications have been limited due to (i) volume expansion during lithiation and delithiation reactions; and (ii) poor conductivity. To cope with that, electrochemical scientists have dedicated wide attention to the development of silicon oxide-carbon (SiO_x/C) composite-based anode materials since it has small volume expansion and high capacity. Importantly, SiO_x/C composite can be produced from zero-cost agricultural waste like rice husk, which makes them viable for commercialization.[1–4]

Over the past few decades, carbonate-based electrolytes such as ethylene carbonate (EC), propylene carbonate (PC), diethyl carbonate (DEC), and dimethyl carbonate (DMC) have been intensively employed in most of the LIBs research. Although they provide excellent electrochemical performance (e.g., high energy density and durable cycling stability), their highly flammable and volatile nature can lead to major safety hazards.[5–8] Hence, exploring liquid electrolytes having high conductivity, low flammability, large mutual solubility with lithium salts, and wide potential window such as ionic liquid and glymes are urgently needed for safety LIBs.

Basically, glymes are poly(ethylene glycol) dimethyl ethers with small *n* number in $R_1O(CH_2CH_2)_nR_2$. They are liquid oligomers which are suitable as aprotic solvents for lithium battery electrolytes.[9] Among safe liquid electrolytes, glyme ones offer advanced properties such as thermal and chemical stabilities across a wide temperature range (100–200 °C), high ionic conductivity (~10^{-3} Scm^{-1}) at room temperature, broad electrochemical potential range (>4 V), low volatility, and less

[a] C. Padwal, L. T. My Hoang, D. Dubal
Centre for Agriculture and the Bioeconomy, Queensland University of Technology, Brisbane, QLD 4000, Australia
E-mail: dubaldeepak2@gmail.com
deepak.dubal@qut.edu.au

[b] C. Padwal, D. Dubal
Centre for Materials Science, School of Chemistry and Physics, Queensland University of Technology, Brisbane, QLD 4000, Australia

[c] H. D. Pham
Centre for Future Materials, University of Southern Queensland, Toowoomba, QLD 4350, Australia
E-mail: hongduc.pham@unisq.edu.au

[d] S. Mundree
School of Agriculture and Food Sustainability, The University of Queensland, Brisbane, QLD 4072, Australia

[e] A. K. Nanjundan
School of Engineering, University of Southern Queensland, Springfield QLD 4300, Australia

[f] S. G. Krishnan
Faculty of Engineering and Information Technology, The University of Melbourne, Victoria 3010, Australia

Supporting information for this article is available on the WWW under https://doi.org/10.1002/cssc.202301866

toxicity and flammability.[9] Even though glyme electrolytes have been studied for LIBs in earlier attempts, the difference between glyme electrolytes (e.g., diglyme and triglyme) with conventional one (e.g., $LiPF_6$) for rice husk-derived SiO_x/C anode was not reported.[6,7,10–12]

Herein, we have investigated the electrochemical performance of SiO_x/C-based anode materials derived from rice husks. Intriguingly, the significant effect of glyme-based electrolytes (such as diglyme and triglyme) on the LIBs' performance was carried out. Briefly, the as-prepared SiO_x/C-based anode material at 1000 °C demonstrated superior electrochemical properties with diglyme electrolyte in comparison with conventional one, which is proven via ex-situ characterizations. Furthermore, the solid-electrolyte-interface (SEI) formation mechanism and composition were uncovered using advanced Time-of-Flight Secondary Ion Mass Spectrometry (ToF-SIMS).

Experimental Details

Synthesis of Silica/Carbon Nanocomposite

Rice husk (SunRice food company, NSW-AU) was pre-treated at 100 °C for 4 h in a deep eutectic solvent that is choline chloride: oxalic acid (1:2) (ChCl: OA) to remove the organic and metal impurities. The pre-treated RH samples were filtered, washed with deionized water, and dried at 80 °C overnight. Consequently, the dried samples were pyrolyzed at three different temperatures 800 °C, 900 °C, and 1000 °C for 120 min (5 °C /min under inert conditions) to synthesize the silica/carbon composites by the carbonization process. The as-prepared samples are symbolized as SiO_x/C@800, SiO_x/C@900, and SiO_x/C@1000, respectively. The synthesized material was washed with 1 M HCl solution to remove impurities and dried in a vacuum oven at 70 °C.

Materials Characterizations

The surface composition was determined by X-ray photoelectron spectroscopy (XPS) measurements using a Kratos AXIS Supra spectrometer. The surface morphology of materials was studied by field emission scanning electron microscopy (FE-SEM) (Tescan-MIRA3), transmission electron microscopy (TEM), and high-resolution TEM (HR-TEM) (JEOL 2100–200 kV) imaging. N_2 adsorption-desorption experiments were carried out to determine the surface area using a Micromeritics 3 Flex instrument. Renishaw Raman microscope was used to obtain the Raman spectra containing a selective laser source at 532 nm of the material. To determine the thermal properties of the nanocomposite, a thermogravimetric analysis (TGA) was carried out using a Netzsch STA 449F3 instrument. The analysis was conducted under an oxygen atmosphere, with a temperature range of 30 to 1000 °C and a heating rate of 10 °C min^{-1}. The conductivity testing instrument (Orion, Thermo Scientific) was used to determine the ionic conductivity of electrolytes.

Electrochemical Characterization

The electrochemical assessment of these SiO_x/C@800, SiO_x/C@900, and SiO_x/C@1000 samples as anode materials in LIBs was conducted using coin-type half-cells (CR2032) assembled in an Ar-filled glovebox. The electrodes were prepared by mixing the active materials (SiO_x/C derivatives) super P and poly (vinylidene fluoride) (PVDF) binders in a weight ratio of 80:10:10 and making a paste using *N*-methyl-2-pyrrolidone (NMP) solution. The paste was cast on copper foil and dried in a vacuum oven at 80 °C for 12 h. The cell comprised Li metal as the counter electrodes, glass microfiber as a separator, and SiO_x/C derivatives. The mass loading was in the range of 0.5 to 0.73 mg over a 12 mm diameter electrode. The electrochemical investigation of the material was performed using different types of electrolytes, such as commercial 1 M lithium hexafluorophosphate ($LiPF_6$) in ethylene carbonate (EC)/dimethyl carbonate (DMC)/diethyl carbonate (DEC) with volume ratio of 1:1:1 (Sigma), and lithium bis(trifluoromethane) sulfonimide (LiTFSI) salt solutions in both diglyme (G2) and triglyme (G3). These cells were cycled between 0.01 and 3.0 V (vs. Li/Li^+). The galvanostatic charge/discharge was performed using Netware battery testers, while cyclic voltammetry was recorded using Biologic VMP-300 potentiostat. Furthermore, fluoroethylene carbonate (FEC) was used as an additive to enhance glyme-based electrolytes' cycling stability. The ex-situ Raman, SEM, and ToF-SIMS analysis were performed.

2. Results and Discussion

2.1. Materials Characterizations

The DES pre-treatment of rice husk was successfully achieved using choline chloride and oxalic eutectic solvents.[2] Furthermore, the temperature parameter was chosen to determine the quality of silica and carbon at three different temperatures from 800 °C, 900 °C, and 1000 °C at a heating rate of 5 °C/min. The RH samples were first pre-treatment using choline chloride and oxalic eutectic solvents as described in our previous report.[2] The samples were then subjected to carbonization at various temperatures. The crystalline nature of the material was determined by XRD analysis (Figure 1a). The SiO_x/C@1000 sample showed an amorphous phase of silica and carbon. Additionally, Bragg's peaks were observed at 18.17°, 28.32°, 37.1°, 41.35°, and 72.5° indicating crystalline phases of silica reporting cristobalite and tridymite reflections due to particles bonding at high temperatures, which was reported previously.[13,14] The silica phase is changed when the temperature increases. While the SiO_x/C@800 provides the amorphous silica phase, SiO_x/C@900 exhibits the transition of the amorphous phase, which was observed at around 70°. Moreover, no impurities are observed in XRD curves. To further investigate the quality of silica and carbon structural quality, Raman analysis was performed. As shown in Figure 1b, strong carbon peaks of 1590 cm^{-1} and 1342 cm^{-1} were found, which are assigned to the G-band (I_G) and D-band (I_D), determining the graphitic carbon correspondingly. Additionally, the broad 2D peak is observed between 2700–2900 cm^{-1}, illustrating the presence of sp2 carbon bond that correlates with graphitic carbon in all three samples. Furthermore, the relative intensity ratio of the peaks, I_D/I_G, is used to calculate the graphitization degree index, which is 0.88, 0.84, and 0.85 in the case of SiO_x/C@800 SiO_x/C@900, and SiO_x/C@1000.

Figure 1c illustrates the TGA of SiO_x/C samples. The weight loss in all samples is associated with the endothermic reaction of moisture evaporation, which occurs in the range of 25 °C–

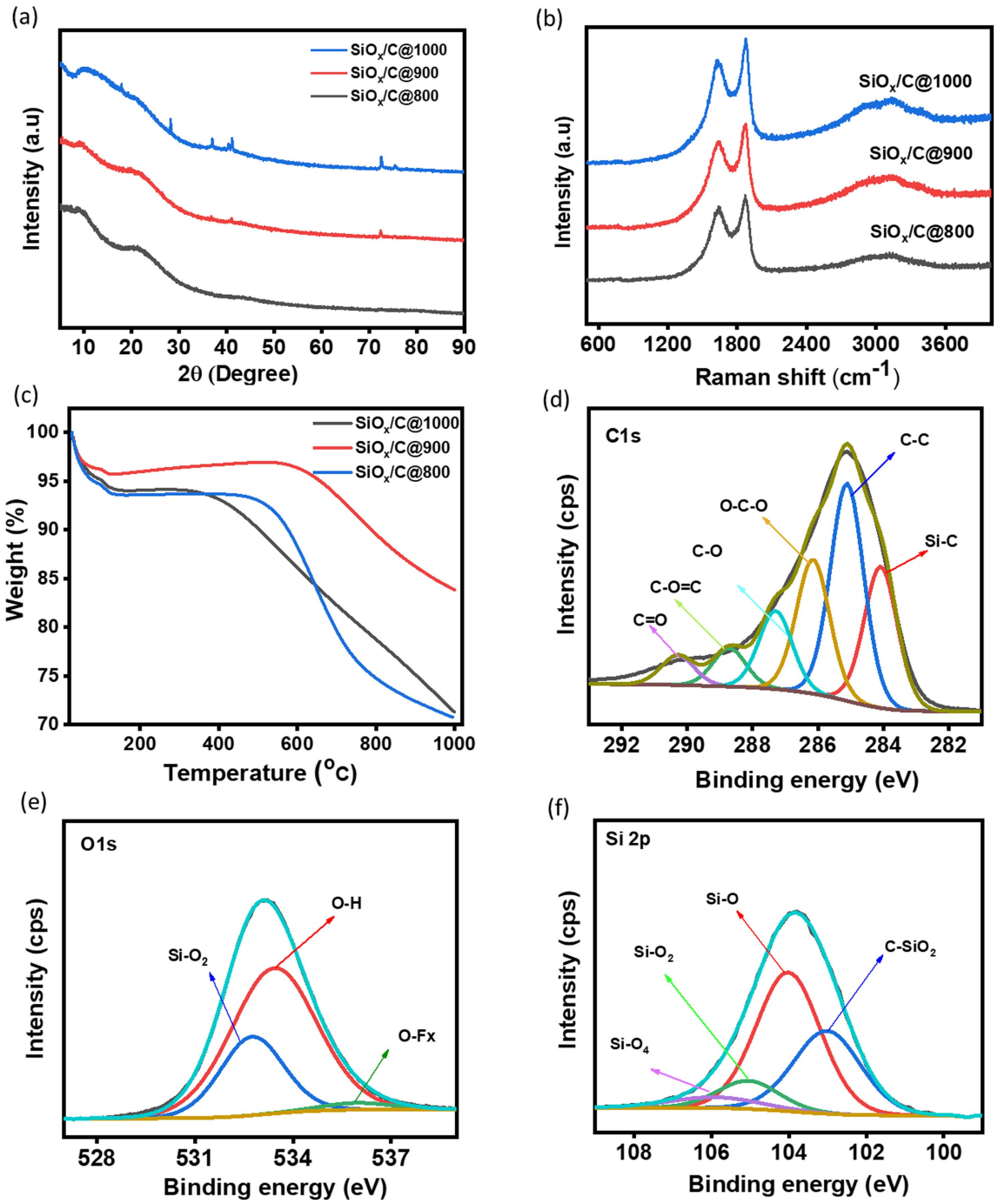

Figure 1. (a) XRD, (b) Raman spectra and (c) TGA of SiO_x/C@1000, SiO_x/C@900 & SiO_x/C@800.

150 °C. The weight loss at this stage was approximately 4.7%. Similar patterns in graph can be noted in the SiO_x/C samples, specifically in the temperature range of 150 °C–600 °C, suggesting an exothermic reaction and a carbon content of about 80–90% in the sample. On the other hand, Between the temperature range of 150 °C–400 °C, the weight loss observed in SiO_x/C@1000 is minimal, and the combined mass of carbon and silica is determined to be 28.7% and 66.6%, respectively, within the temperature range of 400 °C–1000 °C.[15,16] That also ultimately illustrates that the SiO_x/C@1000 contains more silica than other SiO_x/C samples. Figure S2(a–c) depict the BET analysis of the carbonized samples. SiO_x/C@1000 exhibited a higher surface area of 261.44 m^2/g and an average particle pore size of 22.94 nm. Meanwhile, the other two sample comparably showed a lower surface area and larger pore size, for SiO_x/C@800 with 61.90 m^2/g and 96.91 nm, and SiO_x/C@900 with 237.50 m^2/g and 25.26 nm. It can be concluded that the higher the temperature, the better the surface area and pore size, which could possibly make better anodic material.[17]

X-ray photoelectron spectroscopy (XPS) was used for the examination of the elemental composition and chemical states of the samples, with Figure 1 (d–f) illustrating the detailed C 1s, O 1s, and Si 2p spectra for SiO_x/C@1000 samples, and Figure S1 presenting the spectra for SiO_x/C@800 and SiO_x/C@900 samples, as well as a broad spectrum. As shown in the Figure S1., the Si 2p area of the two samples (SiO_x/C@900, SiO_x/C@1000) show similarity with peaks approximately at 106, 104, 105, and 103 eV, which are ascribed to Si–O_4, Si–O_2, Si–O, and C–Si–O_2, respectively. However, the SiO_x/C@800 showed only Si-O_4, Si–O, and C–Si–O_2 spectra. The silicon (Si2p) phase present in all carbonized samples is not just silica but also present in other phases. For SiO_x/C@800 and SiO_x/C@1000 samples, the high-resolution C 1 s spectra fit into five major peaks that may be contributed to Si–C (at 283.1 eV), C–C (at 284.6 eV), O–C–O (at 285.8 eV), C–O (at 286.6 eV), and O–C=O. (at 287.4 eV). Meanwhile, SiO_x/C@900 samples illustrated only the presence of O–C–O, C=O, and C–C. Furthermore, the broad peak at 289.8 eV is attributable to sp2 detected in all three samples. The chemical bonding state of O is shown by the high-resolution O 1s spectra, which correspond to, Si–O_2 (at 532.3 eV), O–H (at 533.4 eV), and O–Fx (at 535,8 eV).

The adsorption-desorption isotherms obtained by Brunauer-Emmett-Teller (BET) analysis (Figure S2, ESI†) suggested that the specific surface areas for SiO_x/C@1000 (261.4 m^2/g), SiO_x/C@900 (237.5 m^2/g) and SiO_x/C@800 (61.4 m^2/g) respectively, Table S2 and Figure S2 summarise silica's total pore volume, specific surface area, and average diameter. The surface morphological analysis is presented in Figure 2(a–c). All of the samples are clusters of circular-shaped particles 50–100 nm linked in the form of closely accumulated nanoparticles and are evenly dispersed all over the carbon surface. In Figure 2(d–f) TEM images agree with SEM images, where we can observe the integration of particles on the carbon surface. Consequently, comparing the carbonization temperature in terms of density and dispersion of nanoparticles, the SiO_x/C@1000 sample looks incomparable as the distribution is more widespread than the other two.

2.2. Electrochemical Study

To investigate the Li^+ storage a behavior of SiO_x/C samples for LIBs using glyme electrolytes, cyclic voltammetry (CV) measurements, GCD tests, cycling tests, rate performance measurements, and EIS were carried out. In-situ and ex-situ experiments were also conducted to elucidate the electrochemical performance. The electrochemical performance of SiO_x/C is investigated in glyme electrolytes and compared with conventional carbonate-electrolyte. The power performance of LIBs is significantly determined by the transport rate of ions in the electrolyte. This rate of the ions is directly proportional to the ion-ion and ion-solvent interaction.[18] In this study, glyme electrolytes are LiTFSI salt solution in both diglyme and triglyme, including 0.1 M, 0.2 M, and 0.4 M LiTFIS in G2 and 0.4 M LiTFSI in G3. Compared to them, the conventional 1 M $LiPF_6$ electrolyte is selected. Since ionic conductivity influences the two major aspects, which are mainly solvation/dissociation and the migration of ion-solvent complexes, the conductivity for all these electrolytes was measured. As shown in Table 1, 1 M $LiPF_6$ possesses the highest ionic conductivity (9.674 mS/cm), followed by 0.4 M G2 (4.78 mS/cm).

All SiO_x/C composite anodes were employed in Li anodic half cells with conventional $LiPF_6$ electrolyte to find the best candidate for further investigation using glyme-based electrolyte. Since the discharge capacity of SiO_x/C@1000 was superior to those of SiO_x/C@800 and SiO_x/C@900 (Figure S4(c–d)), the following parts describe CV and GCD characterization for only SiO_x/C@1000 sample in glyme-based electrolytes.

The Li-ion storage for SiO_x/C@1000 in 0.4 M G2 was tested and illustrated in Figure 3. As shown in Figure 3a, the initial three CV cycles were recorded at a scan rate of 0.2 mVs^{-1} with the voltage ranging from 0.01 V to 3.0 V. The initial cycle showed the broad peaks of the reduction mechanism, which depicts the formation of the SEI layer and the decomposition of the electrolyte. Following the first cycle, these observed peaks vanished, suggesting that the electrode was behaving reversibly and showed a good cycling process. The reduction and oxidation behavior of SiO_x/C@1000 anode in the G2 electrolyte was consistent with those of conventional electrolytes under identical conditions (Figure S3e), suggesting that the conventional electrolyte can be replaced with glyme one for LIBs. The galvanostatic charge/discharge cycling capabilities of the silica/carbon nanocomposites are tested with different electrolytes. Since the focus of the study was to understand glyme-based electrolytes, all SiO_x/C@800, SiO_x/C@900, and SiO_x/C@1000 were initially tested in 0.4 M diglyme electrolyte. Based on the primary test, due to the lower initial reversible capacity of SiO_x/C@800 and SiO_x/C@900 in comparison with that of SiO_x/C@1000, the further electrochemical assessment was focused on SiO_x/C@1000 as it evidently exhibits pure anodic characteristics along with better reversible capacity. Figure S3c illustrated the reversible discharge capacity of SiO_x/C@1000 using conventional LiF6 and 0.4 M G3, which were 469.4 mAh/g and 444.9 mAh/g at 0.04 A/g, respectively. Meanwhile, 0.4 M G2 delivered a specific capacity of 759.7 mAh/g at 0.04 A/g (Figure 3b). Since the electrochemical performance of 0.4 M G2 exhibited better than other ones, the variation of LiTFSI concentration (0.1 M, 0.2 M, and 0.4 M) in G2 was conducted. As shown in Figure S3d, the initial specific discharge capacity of

Table 1. Conductivity Measurements of Electrolytes.

$LiPF_6$ (1 M)	Diglyme (G2)			Triglyme (G3, 0.4 M)
	0.1 M	0.2 M	0.4 M	
9.67 mS/cm	1.24 mS/cm	1.41 mS/cm	4.78 mS/cm	2.56 mS/cm

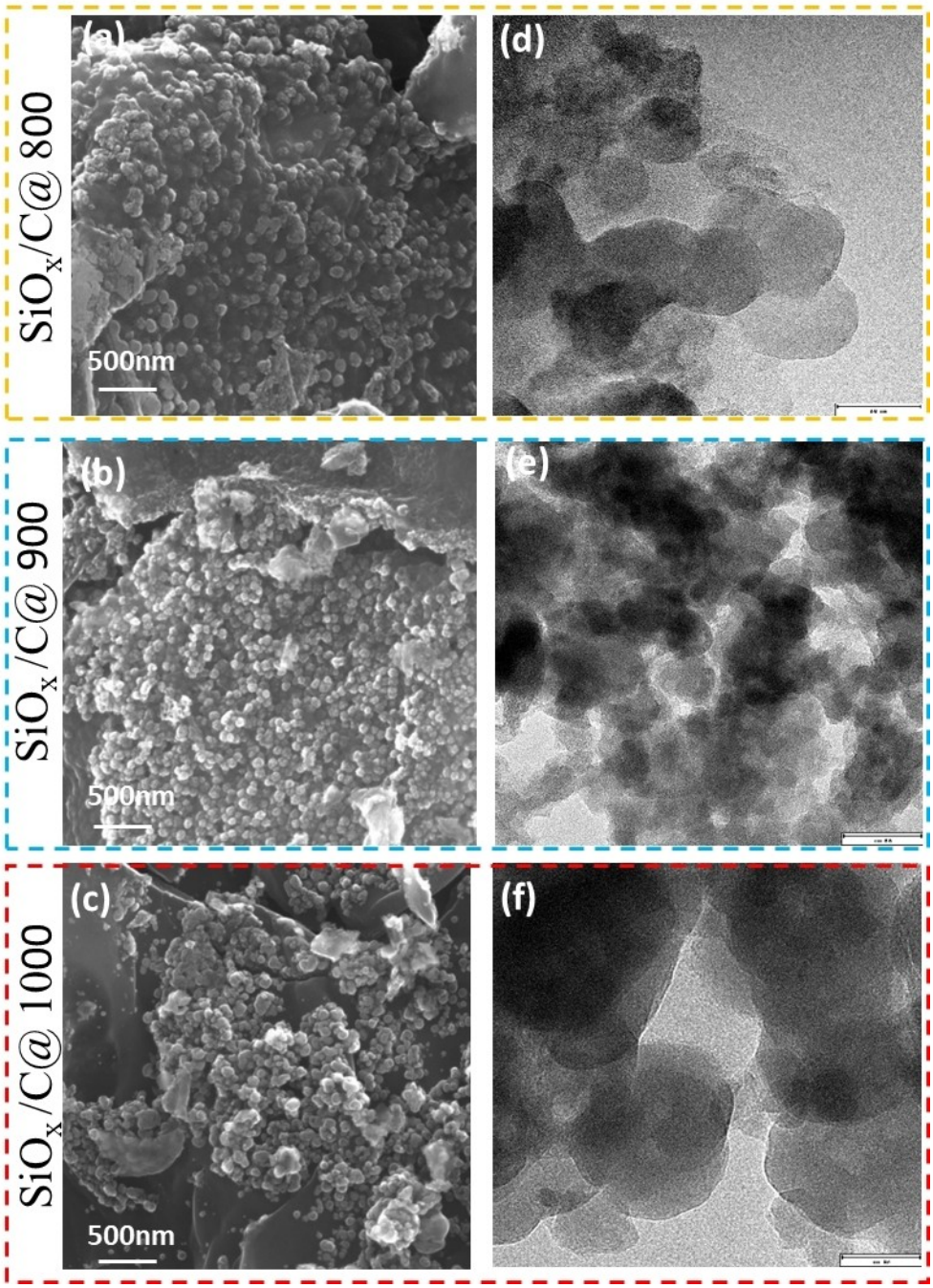

Figure 2. SEM & HR-TEM analysis of SiO_x/C nanocomposite obtained by pre-treated rice husk using ChCl: OA at (a-b) SiO_x/C@ 800, (c-d) SiO_x/C@ 900, (e-f) SiO_x/C@1000.

0.1 M and 0.2 M G2 reached 607.2 and 500.9 mAh/g, respectively, which was lower than that of 0.4 M G2.

The decrease in potential from 1.0 V to 0.3 V in the first lithiation cycle is attributed to the irreversible reduction of the electrolyte, which is consistent with the CV finding. The galvanostatic charge/discharge cycling capabilities of the SiO_x/C nanocomposites are tested in conventional $LiPF_6$, G2 (0.4 M) and G3 (0.4 M). Since the focus of the study was to understand glyme-based electrolytes, materials SiO_x/C@800, SiO_x/C@900, and SiO_x/C@1000 were initially tested in 0.4 M G2. Considering the lower initial reversible capacity of SiO_x/C@800 and SiO_x/C@900, SiO_x/C@1000 was chosen for further electrochemical assessment. Additionally, the reversible discharge capacity was estimated to be 481, 430, and 758 mAh/g for $LiPF_6$, 0.4 M G3, and 0.4 M G2, respectively. For conductivity measurement, $LiPF_6$ shows higher conductivity, which is in agreement with previous studies.[19,20]

The rate performance and stability for SiO_x/C@1000 in 0.4 M G2 electrolyte was carried out. As shown in Figure 3(c–d), the first discharge capacity of 1274 mAh/g and a reversible

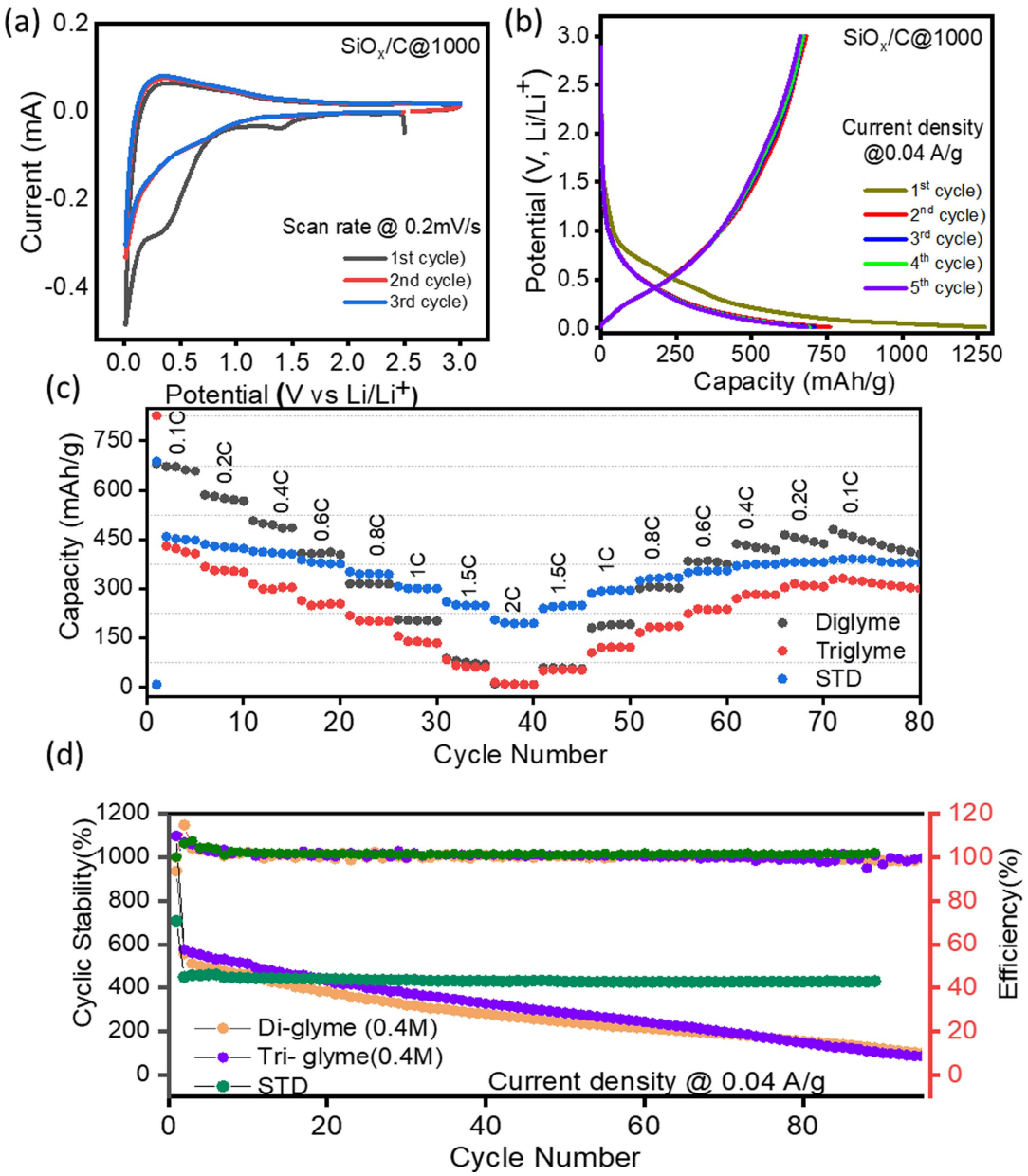

Figure 3. Electrochemical testing of the SiO_x/C@1000 in 0.4 M diglyme, (a)Cyclic voltammetry, (b)GCD, (c) Rate performance of SiO_x/C@1000 in 0.4 M di-glyme, Tri-glyme, and STD electrolyte and (d) Stability plot.

discharge capacity of 759.7 mAh/g were estimated. The initial coulombic efficiency (ICE) was calculated to be 53.4%. After the first irreversible cycle, there was a good match from the second to the fifth cycle, strongly indicating no obvious decrease in charge capacity throughout the first few cycles. The rate performance of the Li half cells with conventional, 0.4 M G2, and 0.4 M G3 electrolytes was conducted under different current rates in the voltage range of 0.01–3.0 V. As illustrated in Figure 3c, the reversible capacities of about 759.7, 624.6, 530.1, 431.3, 328.1, 299.3, 104.8 and 22.1 mAh/g at discharge rates of 0.04, 0.06, 0.08, 0.1, 0.15, 0.2, 0.3, and 0.4 A/g, respectively, were achieved. Notably, when the charge-discharge current rate turns back to 0.04 A/g, the discharge capacities were reduced significantly in comparison with standard $LiPF_6$ electrolyte. This is also demonstrated thorough the cycling stability test (see Figure 3d). After 100 cycles, while the capacity of standard $LiPF_6$ electrolyte retained almost 99%, those of G2 and G3 electrolytes showed a sharp decrease. To cope with that, the SiO_x/C@1000 using 0.4 M G2 electrolyte with 5% and 10% FEC additive was tested. FEC additive is preferred for silicon-based anode materials to enhance the stability.[21] Comparing the first and reversible capacity of the 5% FEC to the 10% in Figure 4(a–c), the 10% exhibited a higher discharge capacity of 497 mAh/g, while the 5% showed a lower capacity of 445 mAh/g with ICE of 58% and 56.61% respectively. The cycling stability of the SiO_x/C@1000 material was then studied, showing excellent stability for the initial 30 cycles with a coulombic efficiency of ~108.33% throughout the entire cycle measurements with

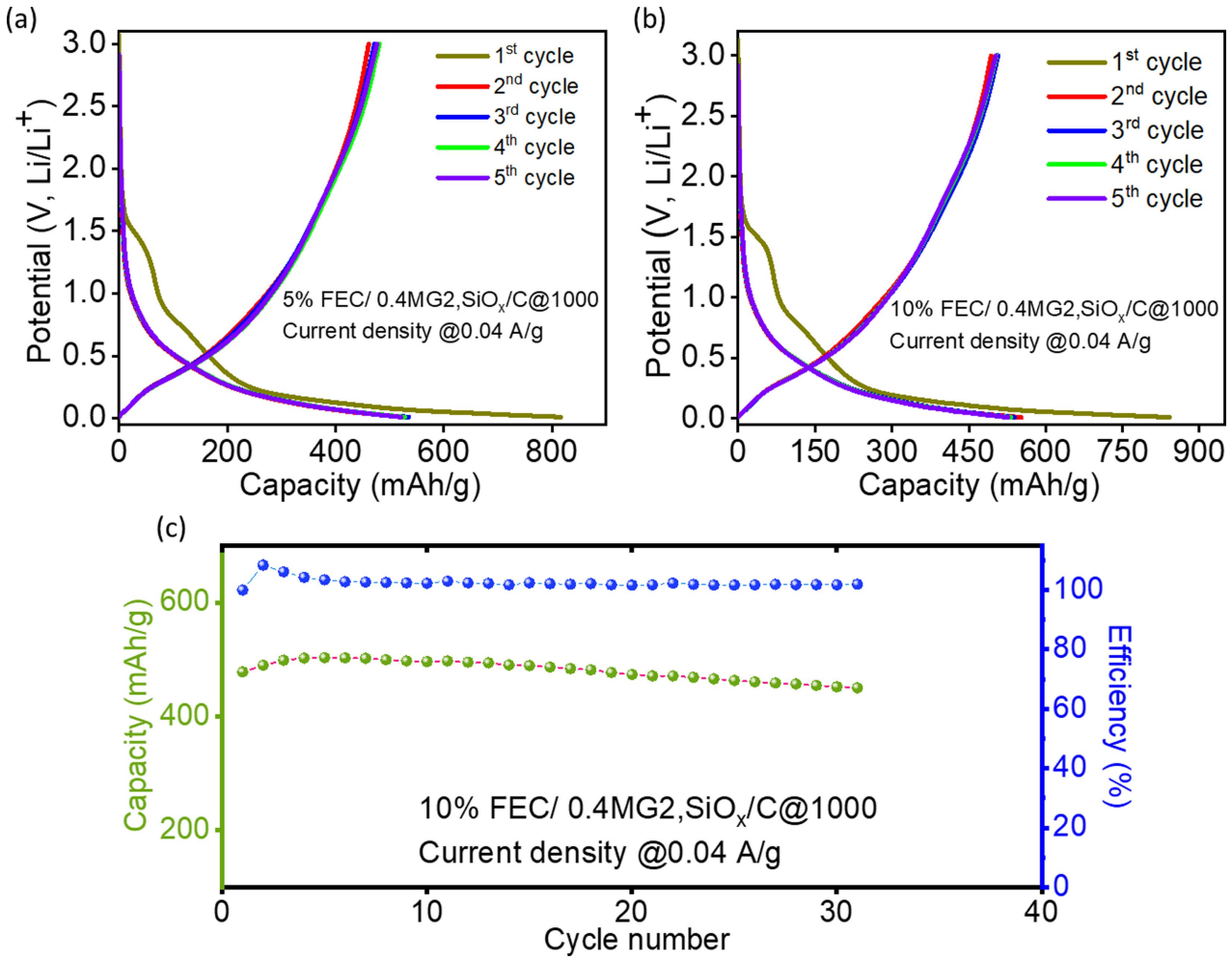

Figure 4. Electrochemical performance of SiO_x/C@1000 in FEC-diglyme electrolyte, (a)GCD of 5% FEC in 0.4 diglyme, (b) GCD of 10% FEC in 0.4 diglyme, (c) Stability of 10% FEC in 0.4 diglyme.

initial discharge capacity of 518 mAh/g. The battery with FEC as an additive showed better stability compared to G2.

The literature also suggested that the primary reason for degradation in cycle life appears to be due to the physical breakdown of the SiO_x/C electrode caused by the expansion and contraction during the charge and discharge of lithium in Si. Another reason for the degradation in the battery life cycle is the impact of the electrolyte solutions. This research has derived material consisting of silica and carbon, the given model explaining the proposed effect of the electrolyte solutions on the charge-discharge of lithium in SiO_x/C electrode. The amorphous SiO_x/C electrode was created by a single-step carbonization method by utilizing post-treated RH, organic residues, and within build silica, the SEM images of the material show the resulting SiO_2 carbon on the electrode surfaces. In glyme electrolyte solutions, lithium ions are selectively solvated by diglyme molecules. During charging, lithium ions, along with solvent molecules, first reach the electrode surface. Due to the amorphous nature of silica, the expansion of silicon molecules is suppressed.[10] Despite the carbon may also serve as the SEI layer which also suppresses the electrolytic and lithium reaction which usually takes place in $LiPF_6$ electrolytic reaction where reactive oxygen species interferes with the battery performance.[22] The pre-lithiation can also help establish a homogeneous and stable SEI layer, which can prevent severe fracture and pulverization of Si-based particles and reduce side reactions between the anode and electrolyte. This, in turn, can result in improved energy density of full cells. Overall, pre-lithiation is a promising approach for improving the performance of lithium-ion batteries and addressing the issue of reduced capacity and energy density due to lithium loss.[23]

The pre-lithiated SiO_x/C@1000 nanocomposite electrode was matched with commercial cathode NMC at a cut-off voltage (4.3 V) to demonstrate full cell performance in 0.4 M G2 electrolyte (Figure S3f) at a current density 0.04 A/g. The initial discharge capacity of the full cell was achieved at 147 mAh/g. Since NMC cathodes possess good storage capacity of Li^+, stable SEI formation with Si based anodes, and high energy density as well as capacity. In the EC-based electrolytes, high voltage cathode material like NMC go through severe side reactions which can accelerate metal dissolution into the electrolyte, pulverization of the cathodic material, and increased

risk of flammability. Whereas high fluorinated glyme-based electrolytes not only provide good performance but have been reported to suppress the flammability of the carbonates, hence aiding the battery safety.[24]

The capacity retention studies of the SiO_x/C electrode were performed in varying current densities from 0.04 to 0.4 A/g. This ten-fold increase in current density would reveal the capacity retention properties of the electrode in different electrolytes (Figure 3c) at different current densities. One could observe that the capacity of the electrode decreases in all the electrolytes and at different current densities. However, the decrease in capacity of the electrode using G2 electrolyte was lower compared to the other two electrolytes. For the G3 and $LiPF_6$ electrolytes, a significant capacity loss was observed after the first activation cycle. However, for the G2 electrolyte, the SiO_x/C electrode shows lower capacity loss in the initial ten cycles at 0.04 mAh/g. The electrode retained 84%, 82%, and 92% of initial reversible discharge capacity at 0.04 mAh/g after 10 charge-discharge cycles. Although the capacity of the electrode decreased with an increase in current density, the stability of the electrode was promising for $LiPF_6$ electrolytes, especially at higher current densities.

The characteristic resistance of the half cell and the charge transfer resistance of the electrode-electrolyte interface after the first cycle are calculated from the EIS studies. The EIS measurements were performed in the frequency range of – MHz to – MHz The Nyquist plot comparing the resistances of the SiO_x/C half-cell employing different electrolytes is compared (-5). In Figure 5, the equivalent circuit for the charge transfer process is modelled using a standard equivalent circuit consisting of a capacitor, resistor, Warburg impedance and constant phase element. The capacitive and resistive measurements will be obtained at higher frequencies whereas Warburg impedance will be obtained at lower frequencies showing the diffusive characteristics of electrode-electrolyte interface. The constant phase element in the circuit removes any surface irregularities in the electrode while measurements. The electrode resistance (R_S) for the SiO_x/C electrode calculated from the x-intercept of the Nyquist plot were 7.4 Ω, 8.8 Ω, and 5.2 Ω, for 0.4 M G2, 0.4 M G3, and $LiPF_6$, respectively. This higher electrode resistance for the Li-ion transfer lowered the performance of diglyme-based SiO_x/C half-cells at higher current densities. Furthermore, the charge transfer resistance (R_{CT}) of the SiO_x/C half-cell calculated from the diameter of a semicircle of the Nyquist plot were 2.4 Ω, 4.3 Ω and 3.4 Ω, 0.4 M G2, 0.4 M G3, and $LiPF_6$ as electrolytes, respectively. This lower charge transfer resistance of the Diglyme electrolyte could have delivered a higher specific capacity at lower current densities. Furthermore, at lower frequencies, the 0.4 M G2 electrolyte based SiO_x/C cell showed a resistance behavior by shifting towards the negative y-axis. However, 0.4 M G3, and $LiPF_6$ cells showed improved diffusion characteristics, which could have resulted in an enhanced rate performance.

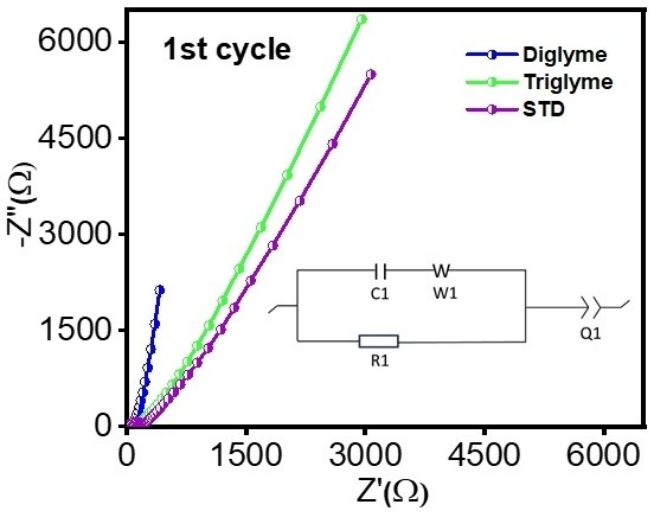

Figure 5. EIS plot of SiO_x/C@1000 electrode cycled with all three electrolytes at 1st cycle along with equivalent circuit.

2.3. Understanding the SEI Layer in Glyme-Electrolytes

To have a better insight into the surface modification of the SiO_x/C@1000 electrode after 50 cycles in three different electrolytes, techniques such as FE-SEM, and ToF-SIMS, Ex-situ analysis was performed. The pristine electrode Figure 6(a–d) shows FE-SEM images, where the uniform distribution of silica/carbon, the particles can be seen intact whereas, have granulated form with carbon chunks. On the other hand, the surface of the electrode cycled for 50 cycles using conventional $LiPF_6$ (EC/DEC/DMC) electrolyte exhibited thick layering, smoother, and homogenous surface. Particularly, visible particles is not observed, which is possibly contributed to the solid electrolyte interfaces (SEIs) formation covered the entire surface.[25] The composition of SEI is directly influenced by the composition of the electrolyte. In carbonate-based electrolytes, the most observed SEI components consist of a mixture of Li_2CO_3 and semi-carbonates (also known as alkyl carbonates).[26,27] Additionally, the specific decomposition products of various solvents depend on the solvent's intrinsic properties, such as reactivity, viscosity, dielectric constant, and polarity. As discussed previously, with the $LiPF_6$-based electrolytes, trace amounts of water can react and generate HF, thereby decomposing key components of SEIs. The porous upper layer is well explained by Zaban et.al,[28] A "multilayered model" was proposed to describe the structure of SEIs. According to this model, the SEI morphology consists of two distinct layers: an inner layer made of compact inorganic compounds like LiF, Li_2O, and Li_2CO_3, and an outer layer containing porous organic compounds such as $(CH_2OCO_2Li)_2$ and LiF. The researchers suggested that the conductivity of the porous organic outer layer is lower compared to the compact inorganic inner layer. As the organic outer layer thickens, it hinders the flow of electrons from the electrode to the electrolyte molecules, preventing further reduction. This self-termination mechanism leads to the cessation of SEI growth. The thickness of the SEI was reported to range from 15 to 100 Å in this model. Furthermore, the cracks on the electrode surface are inclining towards the loss of integrity between Li–Si alloys during de-alloying which ulti-

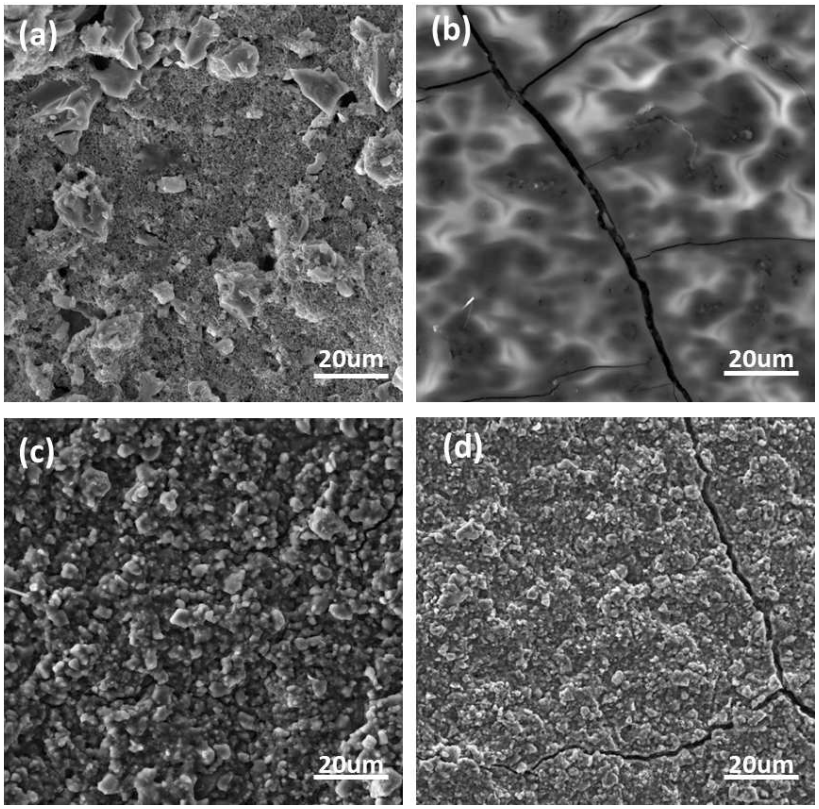

Figure 6. Ex-situ SEM images of SiO_x/C@1000 electrodes tested for 50 cycles in three electrolytes to investigate the surface chemistry (a) Pristine electrode, (b) $LiPF_6$, (c) Di-glyme, (d) Tri-glyme.

mately affects the half-cell capacity which is evident in electrochemical performance. Addition of additives to $LiPF_6$, has been reported ideal to form stable SEI as EC and DEC could lead to cracks in the electrodes and suppress the SEI formation. Etiemble et.al reported that this phenomenon was attributed to the progressive build-up of insoluble degradation products from the electrolyte. It highlights the critical importance of developing more efficient electrolyte formulations to prevent excessive formation of the solid electrolyte interface (SEI) and ensure the feasibility of silicon-based electrodes.[29]

In glyme electrolytes (G2 and G3), the surface of the cycled electrode can be visibly less smother, particle is readily visible, intact, and lesser cracks than that of $LiPF_6$. Comparing early cycles with prolonged cycles in an ether-based electrolytes, there is obvious different effect on SEI. The prolonged cycles have several merits such as reduction of solvent penetration thereby reducing the Si particle swelling. That maintains the higher elasticity compared to the carbonate electrolytes, leading to mitigate the SEI cracking and preventing pulverisation damage. It also endorses higher conductivity of Li ions than the EC based electrolytes. The distribution of SEI in both glyme based electrodes are conformal coating pattern, which promotes uniform lithium transport, resulting in homogenising the volumetric transformation of Si over time preventing from fracturing the SEI.

Another technique for electrode surface chemistry understanding in SEI composition is Time-of-flight secondary ion mass spectrometry (ToF-SIMS).[30–32] This advanced technique plays a vital role in assessing the distribution of components within new microdevices such as lithium metal batteries, particularly in terms of Si-based anode.[33–35] The Figure S7 depicts the wide scan for all the electrodes including pristine, whereas Figure 7–8 depicts the ToF-SIMS data in positive and negative mode for 0.4 M G2 for electrodes cycled for 50 cycles, where isotopes intensity in terms of color distribution and sputter time plot, similarly Figure S6–7 & 10 depicts for $LiPF_6$, and Figure S8–9 & 10 depicts 0.4 M G3. The elements Li and Si composition of 50 times cycled electrodes in pristine electrode, $LiPF_6$, G2 (0.4 M) and G3 (0.4), the results depict Si presence (27.9 m/z) only in pristine electrode than that of all cycled electrodes. On other hand lithium can be observed in $LiPF_6$, G2 (0.4 M) and G3 (0.4) with different levels in intensity counts. Subsequently, along with Li, organic carbonate species in the case of $LiPF_6$ are observed, where hydrocarbons were detected at 14 m/z (CH_2^+), 13 m/z (CH^+) and at 14.9 m/z (CH_3^+). In the initial cycles, the SEI layer is mainly composed of hydrocarbons, PEO-type oligomers, LiF, $LiF_xPF_yO_z$, and $LiF_xPF_yO_z$ products along with the minimum quantity of ethers and alkyl carbonates. The ToF-SIMs for $LiPF_6$ electrolyte illustrated that SEI is formed at the first charging cycle where Li salts in the electrolyte decompose on the anode electrode surface, contributing to the formation of organic and inorganic SEI layer.[36] The surface is primarily made up of low oxidation species LiF(m/z−26), Li_2CO_3 (m/z−90.83), LiOH (m/z−24), Li_2O_2 (m/z−46), LiO (m/z−23.01),

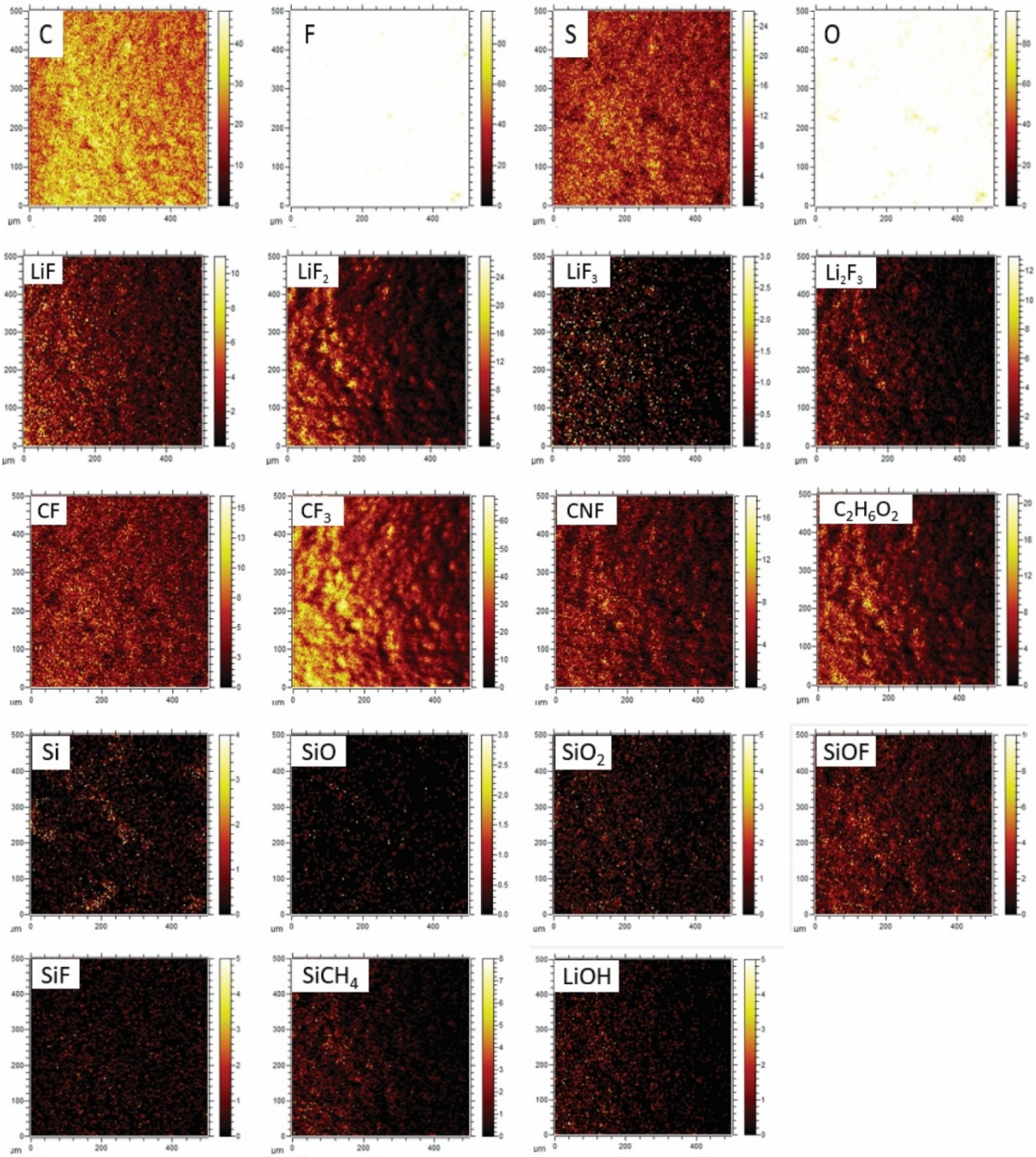

Figure 7. ToF-SIMS analysis in negative ion mode of SiO_x/C@1000 cycled electrodes for 50 cycles in Di-glyme 0.4 M. The element describes the intensity of compounds found on the surface of the electrode. The high intensity can be seen as white and the low intensity is black.

Li_2OH- (m/z−31), Li_2O (m/z−30). Subsequently, the oxidative species like HCOLi (m/z−36), CH_3COLi (m/z−57), $CH_2CH_2OCH_2Oli$ (m/z−81) are mainly found on surface layer of SEI and can be seen in positive mode (Figure S7). In the case of diglyme and tri-glyme electrolytes, showed the absence of Li_2CO_3, and other carbonates residues.

The hydrolysis of $LiPF_6$ is strongly coordinated by PF^{6-} (m/z−144.96) anion, present in the solvent and stimulated through electrostatic interactions between fluorine atoms present in the vicinity. Following is the reaction illustrating the $LiPF_6$ dissociation reactions.

$$LiPF_6 \rightleftharpoons Li + +PF_6 \quad (1)$$

$$LiPF_6 \rightleftharpoons PF_5 + LiF \quad (2)$$

$$PF_5 + H_2O \rightleftharpoons POF_3 + 2HF \quad (3)$$

$$LiPF_6 + H_2O \rightleftharpoons POF_3 + 2HF + LiF \quad (4)$$

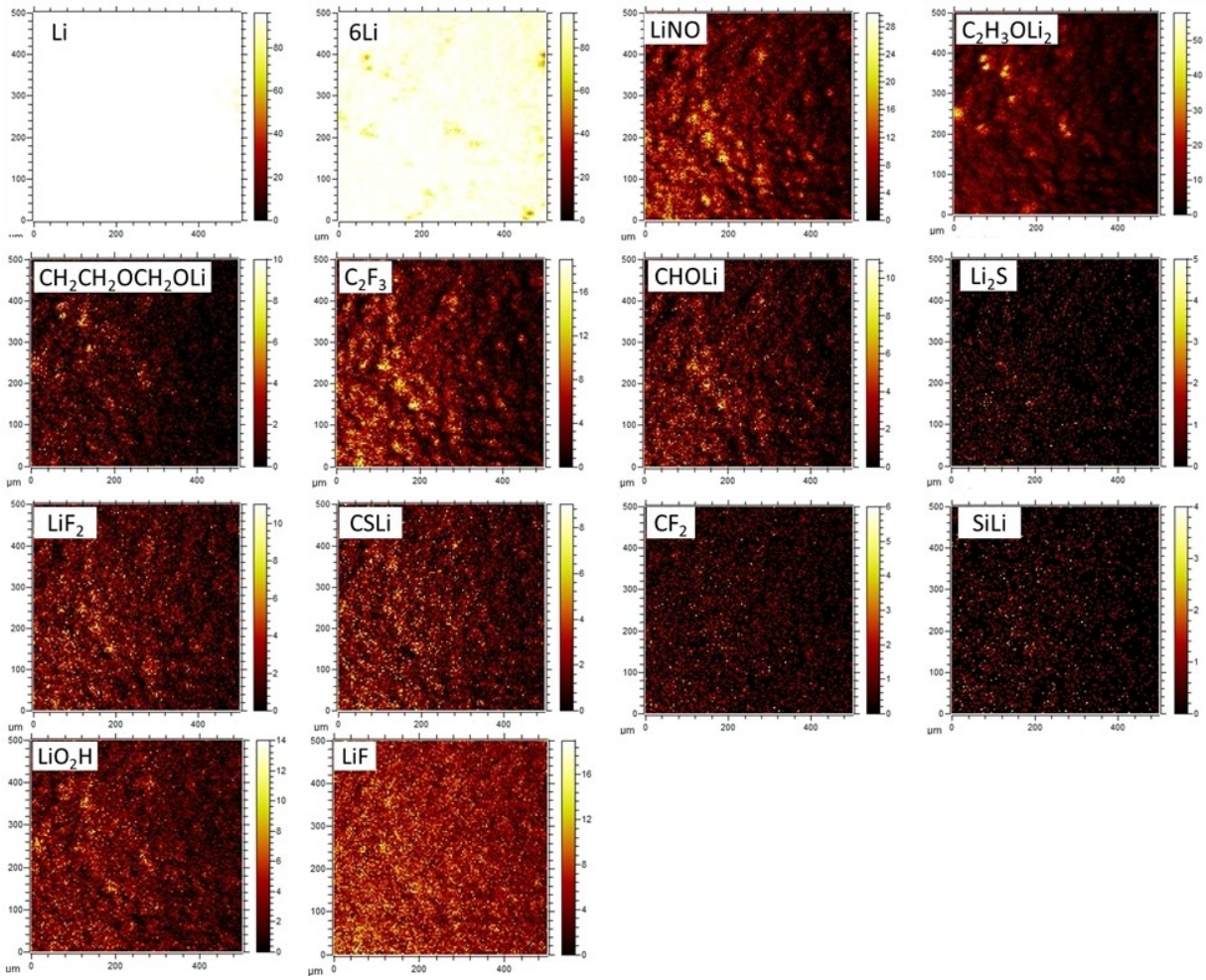

Figure 8. ToF-SIMS analysis in Positive ion mode of SiO_x/C@1000 cycled electrodes for 50 cycles in Di-glyme 0.4 M. The element describes the intensity of compounds found on the surface of the electrode. The high intensity can be seen as white and the low intensity is black.

$$LiPF_{6+}H_2O \rightleftharpoons PF_5 + HF + LiOH \quad (5)$$

The calculated Gibbs energy of reaction 2 and 3 is 64 kJ/mol and 92 kJ/mol,[37] the reaction 2 is driven by Li+ solvation in dielectric media, however reaction 3 is considered negligible at lower than 60 °C due to the higher values of reaction energy which leads to thermal aging of electrolyte in the presence of water and PF_6, resulting in HF production. The trace amount of HF and its derivative can contribute towards probable alteration in Li–Si alloy formation and composition. Furthermore, occurrence of LiOH through water and electrolyte interaction takes place making it major component of SEI. The presence of LiF (m/z−26), LiOH (m/z−24), 2HF (m/z−21) and PF_6 is justifying the reaction and deposition on electrode contributing towards SEI which is measured on the surface of electrode.[36]

Similarly, the dissociation reaction of LiTFSI shown in below reactions (3-1) is coordinated by the TFSI anion by coulombic interactions takes place amongst metal ions, a positively charged and sulphonyl groups, negatively charged. The surface profiling shows the presence of LiF on SEI layer of all electrolytes, however PF_6 (m/z−144.96) is only seen in $LiPF_6$, respectively.

$$LiTFSI + H_2O \rightleftharpoons HTFSI + LiOH(s) \quad (6)$$

$$LiTFSI + H_2O \rightleftharpoons HTFSI + LiOH(sol) \quad (7)$$

$$HTFSI \rightleftharpoons C_2F_5NO_4S_2 + HF \quad (8)$$

$$LiTFSI + HF \rightleftharpoons HTFSI + LiF(s) \quad (9)$$

In the TFSI hydrolysis, precipitation of LiOH occurs at the same time as solvated HTFSI [6], the fluorine atom from $-CF_3$ (m/z−69) is expensive thermodynamically because of the C–F bond covalent interaction. The $C_2F_5NO_4S_2$ released in the reaction 8, becomes the barrier in production of high amount of HF due to lower gibs energy 63 kJ/mol due to possible kinetic activation energy. Therefore, in case if TFSI, HF released in the process of hydrolysis is strongly limited in comparison with $LiPF_6$. ToF-SIMs data justifies the absence of HF in case of G2 and G3 shows presence of all –CF (m/z−16), $-CF_3$ (m/z−69), $+C_2F_3$ (m/z−81) isotopes.[36]

The signal intensities decomposition products mainly observed in TFSI are (m/z−36), CH_3COLi_2 (m/z−57), $CH_2CH_2OCH_2OLi$ (m/z−81), and Li_2OH (m/z−31), tend to

decrease as the inorganic phase components from the TFSI reaction shows enhanced intensities. Some products of lithium salts dissociation in inorganic phase was observed in both ion modes, are LiF (m/z−26), LiF_2, (m/z−45), LiF_3 (m/z−64), Li_2F_3 (m/z−33), Li_2S (m/z−46), CSLi (m/z−51), LiNO (m/z−37), these results shows that the diglyme SEI consist of both organic and inorganic bilayer assembly. The presence of more Li–F based compounds on surface evenly distributed on SEI layer is observed better in G2 amongst the electrolyte (Figure 8–9). It also illustrates the more straightforward reduction of anions, a high electronegativity of fluorine in LiTFSI, leading to stale SEI layer.[36–39] The G2 also shows the isotopes of Si based compound and high intensity than other two electrolytes. The sputter plots explain the intensities of respective compounds present on the on the surface with respect to the time of flight and measured using primary beam (Bi). The sputtering time and signal intensity of element F and C and its compounds can be used to estimate the strength of the interfacial layer. As sputtering time increases, the signal of element is significantly consistent, indicating that the SEI is mainly composed of an inorganic phase from the surface to the inner layer.[36] In Figure 9 and S10 explains the compounds strength on the SEI layer electrode for G2, G3 and $LiPF_6$.

3. Conclusions

In summary, we have successfully demonstrated that the glyme-based electrolytes are promising for Li-ion battery technology. The as-synthesized SiO_x/C nanocomposite electrode demonstrate a reversible discharge capacity of 759.7 mAh/g in di-glyme electrolyte at 0.04 A/g. Furthermore, reversible retention capacity was achieved at 71% at 0.04 A/g after 10 cycles which ultimately affects the rate capability of the battery. Subsequently, integrating 10% FEC in 0.4MG2 showed stable discharge capacity than only G2 (0.4 M) upon cycling. Performing ex-situ analysis of cycled electrolyte by ToF-SIMS and SEM allows to evident the comparative study of electrolyte. The conventional based cycled electrode shows thick film layer of SEI which affects the ion diffusion and shows presence of carbonates which affects the performance as well as induces reactive species. The electrode in glyme based electrolyte shows stable structure and surface of electrode even after 50 cycles. The ToF-SIMS data explains the surface compound characteristics of inner and outer layer. The presence of HF in $LiPF_6$ explains the capacity drop in GCD due to involving in Li–Si alteration mechanism. The diglyme showed best SEI layer and presence of diverse LiF, CF, Si isotopes-based compounds which fulfills the criteria of good quality SEI layer.

Acknowledgements

C.P. is thankful to QUT-Centre for Agriculture and the Bioeconomy (CAB) for the QUTPRA scholarship for conducting her doctoral research. The authors acknowledge Dr. Rob Jones, Senior Research infrastructure Specialist, for his assistance for ToF-SIMS analysis, and the facilities, and the scientific and technical assistance of staff at Central Analytical Research Facility (CARF). D.P.D. acknowledges the financial support from Centre for Materials Science and Centre for Waste Free World, QUT, Australia. Open Access publishing facilitated by Queensland University of Technology, as part of the Wiley - Queensland University of Technology agreement via the Council of Australian University Librarians.

Conflict of Interests

The authors declare no conflict of interest.

Keywords: silicon-based anode · electrolyte · glyme · Time-of-Flight Secondary Ion Mass Spectrometry · lithium-ion batteries

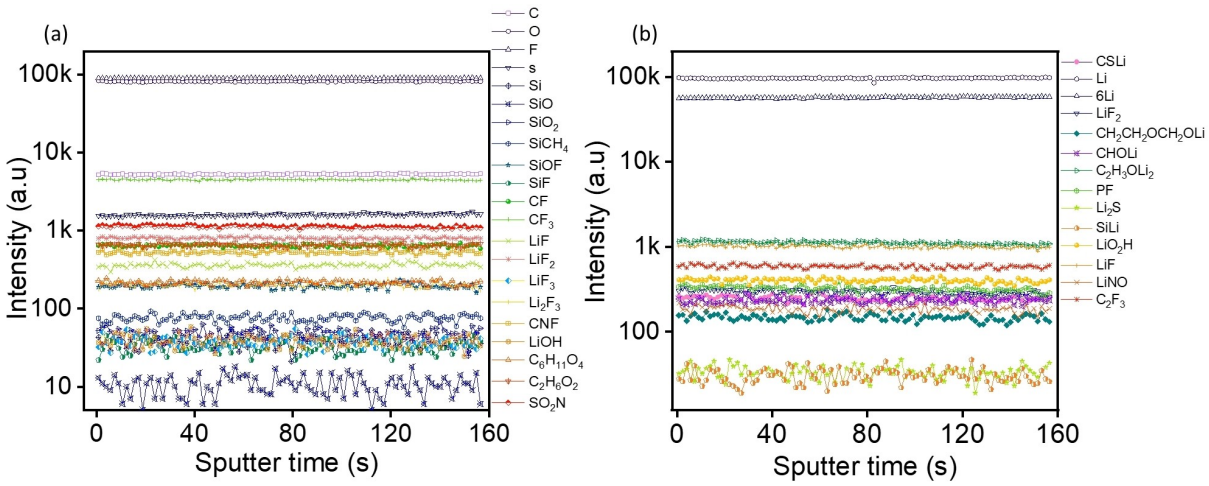

Figure 9. ToF-SIMS analysis in negative ion mode of SiO_x/C@1000 cycled electrodes for 50 cycles in Di-glyme 0.4 M. The graph illustrates the intensity of compounds scanned on the electrode surface to determine SEI composition with respect to time, and the respective type of compound can be seen with a colored line.

[1] H. Chu, Q. Wu, J. Huang, *Colloids Surf. A* **2018**, *558*, 495.
[2] C. Padwal, H. D. Pham, L. T. M. Hoang, S. Mundree, D. Dubal, *Sustainable Materials and Technologies* **2023**, *35*, e00547.
[3] M. Yang, L. Jin, M. He, Z. Yi, T. Duan, W. Yao, *Appl. Surf. Sci.* **2021**, *542*, 148712.
[4] N. Liu, K. Huo, M. T. McDowell, J. Zhao, Y. Cui, *Sci. Rep.* **2013**, *3* (1), 1919.
[5] P. Jaumaux, J. Wu, D. Shanmukaraj, Y. Wang, D. Zhou, B. Sun, F. Kang, B. Li, M. Armand, G. Wang, *Adv. Funct. Mater.* **2021**, *31* (10), 2008644.
[6] S. Tobishima, H. Morimoto, M. Aoki, Y. Saito, T. Inose, T. Fukumoto, T. Kuryu, *Electrochim. Acta* **2004**, *49* (6), 979.
[7] S. Wei, Z. Li, K. Kimura, S. Inoue, L. Pandini, D. Di Lecce, Y. Tominaga, J. Hassoun, *Electrochim. Acta* **2019**, *306*, 85.
[8] J. Clarke-Hannaford, M. Breedon, T. Ruther, M. J. Spencer, *ACS Appl. Energ. Mater.* **2020**, *3* (6), 5497.
[9] Z. Zeng, V. Murugesan, K. S. Han, X. Jiang, Y. Cao, L. Xiao, X. Ai, H. Yang, J.-G. Zhang, M. L. Sushko, *Nat. Energy* **2018**, *3* (8), 674.
[10] T. Inose, D. Watanabe, H. Morimoto, S.-I. Tobishima, *J. Power Sources* **2006**, *162* (2), 1297.
[11] M. Nojabaee, J. Popovic, J. Maier, *J. Mater. Chem. A* **2019**, *7* (21), 13331.
[12] S. Parveen, P. Sehrawat, S. Hashmi, *ACS Appl. Energ. Mater.* **2021**, *5* (1), 930.
[13] E. Rohaeti, I. Hikmawati, *J. Mater. Sci. Technol.* **2010**, 265–272, ISBN 978-602-97444-3-9.
[14] J.-J. F. Saceda, R. L. d. Leon, K. Rintramee, S. Prayoonpokarach, J. Wittayakun, *synthesis. Quim. Nova* **2011**, *34*, 1394.
[15] I. Y. Tishchenko, O. Ilchenko, P. Kuzema, *Chem. Phys. Technol. Surf* **2015**, *6*, 216.
[16] V. T. Phat, C. T. M. Thu, N. T. Trung, L. M. L. Phung, W. Kaveevivitchai, T. Van Man, *Int. J. Energy Res.* **2022**, *46* (15), 21727.
[17] J. Cui, F. Cheng, J. Lin, J. Yang, K. Jiang, Z. Wen, J. Sun, *Powder Technol.* **2017**, *311*, 1.
[18] S. Hwang, D.-H. Kim, J. H. Shin, J. E. Jang, K. H. Ahn, C. Lee, H. Lee, H *J. Phys. Chem. C* **2018**, *122* (34), 19438.
[19] J. G. Han, K. Kim, Y. Lee, N. S. Choi, *Adv. Mater.* **2019**, *31* (20), 1804822.
[20] J. Gnanaraj, E. Zinigrad, L. Asraf, H. Gottlieb, M. Sprecher, M. Schmidt, W. Geissler, D. Aurbach, *J. Electrochem. Soc.* **2003**, *150* (11), A1533.
[21] J. Ko, Y. S. Yoon, *Ceram. Int.* **2019**, *45* (1), 30.
[22] J. O. Besenhard, *Handbook of battery materials*, John Wiley & Sons, **2008**, 56–57.
[23] T. Jia, G. Zhong, Y. Lv, N. Li, Y. Liu, X. Yu, J. Zou, Z. Chen, L. Peng, F. Kang, *Green Energy & Environment* **2022**, *8*(5), 1325–1340.
[24] X. Fan, C. Wang, *Chem. Soc. Rev.* **2021**, *50* (18), 10486.
[25] S. Balamurugan, N. Naresh, I. Prakash, N. Satyanarayana, *Appl. Surf. Sci.* **2021**, *535*, 147677.
[26] Y. Domi, M. Ochida, S. Tsubouchi, H. Nakagawa, T. Yamanaka, T. Doi, T. Abe, Z. Ogumi, *J. Phys. Chem. C* **2011**, *115* (51), 25484.
[27] Y. Chu, Y. Shen, F. Guo, X. Zhao, Q. Dong, Q. Zhang, W. Li, H. Chen, Z. Luo, L. Chen, *Electrochemical energy reviews* **2020**, *3*, 187.
[28] A. Zaban, D. Aurbach, *J. Power Sources* **1995**, *54* (2), 289.
[29] A. Etiemble, A. Tranchot, T. Douillard, H. Idrissi, E. Maire, L. Roué, *J. Electrochem. Soc.* **2016**, *163* (8), A1550.
[30] D. Wu, C. Zhu, H. Wang, J. Huang, G. Jiang, Y. Yang, G. Yang, D. Tang, J. Ma, *Angew. Chem. Int. Ed.* **2024**, *63* (7), e202315608.
[31] J. Liu, X. Li, J. Huang, G. Yang, J. Ma, *Adv. Funct. Mater.* **2024**, 2312762.
[32] H. Wang, J. Liu, G. Jiang, J. Huang, D. Wu, G. Yang, J. Ma, *Adv. Energy Mater.* **2024**, 2400067.
[33] J. Wu, M. Ihsan-Ul-Haq, Y. Chen, J.-K. Kim, *Nano Energy* **2021**, *89*, 106489.
[34] Y. Li, Z. Cao, Y. Wang, L. Lv, J. Sun, W. Xiong, Q. Qu, H. Zheng, *ACS Energy Lett.* **2023**, *8*, 4193.
[35] S. Park, S. Kim, J.-A. Lee, M. Ue, N.-S. Choi, *Chem. Sci.* **2023**, *14* (37), 9996.
[36] C. Ma, F. Xu, T. Song, *ACS Appl. Mater. Interfaces* **2022**, *14* (17), 20197.
[37] S. Di Muzio, A. Paolone, S. Brutti, *J. Electrochem. Soc.* **2021**, *168* (10), 100514.
[38] W. Huang, Y. Wang, L. Lv, G. Zhu, Q. Qu, H. Zheng, *Energy Storage Mater.* **2022**, *52*, 646.
[39] Z.-Y. Wu, L. Deng, J.-T. Li, S. Zanna, A. Seyeux, L. Huang, S.-G. Sun, P. Marcus, J. Światowska, *Batteries* **2022**, *8* (12), 271.

Manuscript received: December 13, 2023
Revised manuscript received: April 1, 2024
Accepted manuscript online: April 3, 2024
Version of record online: May 6, 2024